

THERMAL STRUCTURE AND COOLING OF SUPERFLUID NEUTRON STARS WITH ACCRETED MAGNETIZED ENVELOPES

ALEXANDER Y. POTEKHIN,^{1,2} DMITRY G. YAKOVLEV,¹ GILLES CHABRIER,³ AND OLEG Y. GNEDIN⁴

Received 2003 February 21; accepted 2003 May 13

ABSTRACT

We study the thermal structure of neutron stars with magnetized envelopes composed of accreted material, using updated thermal conductivities of plasmas in quantizing magnetic fields, as well as the equation of state and radiative opacities for partially ionized hydrogen in strong magnetic fields. The relation between the internal and local surface temperatures is calculated and fitted by an analytic function of the internal temperature, magnetic field strength, angle between the field lines and the normal to the surface, surface gravity, and the mass of the accreted material. The luminosity of a neutron star with a dipole magnetic field is calculated for various values of the accreted mass, internal temperature, and magnetic field strength. Using these results, we simulate cooling of superfluid neutron stars with magnetized accreted envelopes. We consider slow and fast cooling regimes, paying special attention to very slow cooling of low-mass, superfluid neutron stars. In the latter case, the cooling is strongly affected by the combined effect of magnetized accreted envelopes and neutron superfluidity in the stellar crust. Our results are important for the interpretation of observations of the isolated neutron stars hottest for their age, such as RX J0822–43 and PSR B1055–52.

Subject headings: dense matter — magnetic fields —
stars: individual (PSR B1055–52, RX J0822–4300) — stars: neutron

1. INTRODUCTION

The cooling of neutron stars (NSs) depends on the properties of dense matter in their crusts and cores. Theoretical predictions of these properties depend on the model of strong interaction and the many-body theory employed. Therefore, one can test microscopic models of dense matter by comparing the results of simulations of NS cooling with observations of the stellar thermal emission (see, e.g., Pethick 1992; Page 1997, 1998). The history of NS cooling theory is reviewed by, e.g., Yakovlev, Levenfish, & Shibano (1999); the main cooling regulators are discussed by, e.g., Yakovlev et al. (2002a). Practical implementation of this method is restricted by the accuracy of observational data and by the quality of the physics input used in calculations.

It is conventional (see, e.g., Gudmundsson, Pethick, & Epstein 1983) to separate the outer *heat-blanketing envelope* from the stellar interior. The blanketing envelope can be treated separately in the plane-parallel quasi-Newtonian approximation (Gudmundsson et al. 1983), which simplifies the cooling calculations.

NS cooling is strongly affected by the relation between the heat flux density F and the temperature at the inner boundary of the blanketing envelope T_b . The flux density is constant throughout a given local part of the envelope. It is conventionally written as $F = \sigma T_s^4$, where T_s is the local effective surface temperature and σ is the Stefan-Boltzmann

constant. The T_b - T_s relation is determined by the equation of state (EOS) and thermal conductivity of matter in the heat-blanketing envelope.

For nonmagnetized stellar envelopes composed of iron, this relationship was thoroughly studied by Gudmundsson et al. (1983). Chabrier, Potekhin, & Yakovlev (1997) and Potekhin, Chabrier, & Yakovlev (1997, hereafter Paper I), reconsidered the problem and extended the results in two aspects. First, advanced theoretical data on EOS and thermal conductivity allowed the authors to study colder NSs, with T_s down to 5×10^4 K. Second, the authors considered blanketing envelopes composed not only of iron but also of light (accreted) elements. They found that a small amount of accreted matter (with mass $10^{-16} M_\odot \lesssim \Delta M \lesssim 10^{-7} M_\odot$) results in higher T_s at a given T_b . As a consequence, the stellar luminosity is higher at the early (neutrino-dominated) cooling stage (at stellar ages $t \lesssim 10^4$ – 10^5 yr) and lower at the subsequent photon stage.

Recently, the thermal structure of accreted envelopes has been studied by Brown, Bildsten, & Chang (2002), taking into account that hydrogen burning in accreted matter may proceed (Schatz et al. 2001) far beyond Fe (up to Te) via the rapid proton capture process.

It was realized long ago (Tsuruta et al. 1972) that strong magnetic fields can greatly affect the surface temperature and cooling of NSs. The thermal structure of NS envelopes with radial magnetic fields (normal to the surface) was studied by Van Riper (1988 and references therein). His principal conclusion was that the field reduces the thermal insulation of the blanketing envelope as a result of Landau quantization of electron motion.

The thermal structure of the envelope with magnetic fields normal and tangential to the surface was analyzed by Hernquist (1985) and Schaaf (1990a). The tangential field increases the thermal insulation of the envelope, because the Larmor rotation of the electrons reduces the transverse electron thermal conductivity.

¹ Ioffe Physico-Technical Institute, Politekhnicheskaya 26, 194021 St. Petersburg, Russia; palex@astro.ioffe.ru, yak@astro.ioffe.ru.

² Isaac Newton Institute of Chile, St. Petersburg Branch, St. Petersburg, Russia.

³ Ecole Normale Supérieure de Lyon (CRAL, UMR CNRS 5574), 46 allée d'Italie, 69364 Lyon Cedex 07, France; chabrier@ens-lyon.fr.

⁴ Space Telescope Science Institute, 3700 San Martin Drive, Baltimore, MD 21218; ognedin@stsci.edu.

The case of arbitrary angle θ between the field lines and the normal to the surface was studied by Greenstein & Hartke (1983) in the approximation of constant (density- and temperature-independent) longitudinal and transverse thermal conductivities. The authors proposed a simple formula that expresses T_s at arbitrary θ through two values of T_s calculated at $\theta = 0^\circ$ and 90° . The case of arbitrary θ was studied also by Schaaf (1990b) and Heyl & Hernquist (1998, 2001).

Potekhin & Yakovlev (2001, hereafter Paper II) reconsidered the thermal structure of the blanketing envelopes for any θ , using improved thermal conductivities (Potekhin 1999). In agreement with an earlier conjecture of Hernquist (1985) and simplified treatments of Page (1995) and Shibanov & Yakovlev (1996), Paper II demonstrated that the dipole magnetic field (unlike the radial one) does not necessarily increase the total stellar luminosity L_γ at a given T_b . On the contrary, the field with $B \sim 10^{11}$ – 10^{13} G lowers L_γ , and only the fields with $B \gtrsim 10^{14}$ G significantly increase it.

Early simulations of cooling of magnetized NSs were performed assuming the radial magnetic field everywhere over the stellar surface (see, e.g., Tsuruta et al. 1972; Nomoto & Tsuruta 1987; Van Riper 1991). Since the radial magnetic field reduces the thermal insulation, these models predicted the increase of L_γ by the magnetic field at the neutrino cooling stage. Page (1995) and Shibanov & Yakovlev (1996) simulated cooling of NSs with dipole magnetic fields, using the Greenstein-Hartke formula and the T_b - T_s relations at the magnetic pole and equator taken from the previous work (Hernquist 1985; Van Riper 1988; Schaaf 1990a). Heyl & Hernquist (1997a, 1997b, 1998, 2001) proposed simplified models of cooling magnetized NSs, including the cases of ultrahigh surface magnetic fields, $B \sim 10^{15}$ – 10^{16} G. Recently, the improved T_b - T_s relation derived in Paper II has been used for simulating the cooling of NSs with dipole magnetic fields (Paper II; Kaminker, Yakovlev, & Gnedin 2002; Yakovlev et al. 2002a).

Most of the above-cited work on magnetized NSs has been focused on NSs with iron envelopes, except that Heyl & Hernquist (1997a) have used simplified analytic models to calculate cooling of ultramagnetized ($B \sim 10^{15}$ – 10^{16} G) NSs that may possess accreted envelopes.

In this paper, we consider accreted NS envelopes (as in Paper I for $B = 0$), but take into account strong magnetic fields B directed at various angles θ (as in Paper II for iron envelopes). We use the modern electron conductivities of magnetized envelopes (Potekhin 1999), taking into account the effects of the finite size of atomic nuclei, appropriate for the inner envelopes (Gnedin, Yakovlev, & Potekhin 2001), as well as the radiative opacities and EOS of strongly magnetized, partially ionized hydrogen in NS atmospheres (Potekhin & Chabrier 2003). We derive an analytic approximation for the surface temperature. We calculate T_{eff} for a dipole magnetic field and simulate NS cooling to demonstrate the effects of magnetic fields and accreted envelopes on thermal evolution of NSs.

In § 2, we give an overview of the main effects of strong magnetic fields on heat conduction in a plasma and introduce basic definitions. In § 3, we describe the physics input used in our simulations. The thermal structure of NS envelopes with magnetic fields is discussed in § 4. NS cooling simulations are presented in § 5. The conclusions are formulated in § 6.

2. THE EFFECTS OF STRONG MAGNETIC FIELDS ON HEAT CONDUCTION IN NS ENVELOPES

We call a magnetic field *strong* if the electron cyclotron energy $\hbar\omega_c = \hbar eB/m_e c$ exceeds 1 a.u.—i.e., the field strength B is higher than $m_e^2 c^3 / \hbar^3 = 2.3505 \times 10^9$ G, where m_e is the electron mass, e the elementary charge, and c the speed of light. We call the field *superstrong* if $\hbar\omega_c > m_e c^2$, that is, $B > m_e^2 c^3 / e\hbar = 4.414 \times 10^{13}$ G.

The field is called *strongly quantizing* if it sets almost all electrons on the ground Landau level. The latter case takes place at temperature $T \ll T_B$ and density $\rho < \rho_B$, where

$$\rho_B = m_u n_B \langle A \rangle / \langle Z \rangle \approx 7045 B_{12}^{3/2} (\langle A \rangle / \langle Z \rangle) \text{ g cm}^{-3} \quad (1)$$

and

$$T_B = \hbar\omega_c / k_B \approx 1.343 \times 10^8 B_{12} \text{ K} . \quad (2)$$

Here $m_u = 1.66054 \times 10^{-24}$ g is the atomic mass unit, $\langle A \rangle$ and $\langle Z \rangle$ are the mean ion mass and charge numbers, respectively, $B_{12} \equiv B / (10^{12} \text{ G})$, $n_B = 1 / (\pi^2 \sqrt{2} a_m^3)$ is the electron number density at which the electron Fermi energy reaches the first excited Landau level, and $a_m = (\hbar c / eB)^{1/2}$ is the quantum magnetic length.

As a rule, at $\rho > \rho_B$ and not too high a T , the electron thermodynamic and kinetic functions oscillate, with increasing ρ , around their values calculated neglecting quantization of electron motion in Landau levels. If $T \gtrsim T_B$ or $\rho \gg \rho_B$, the field can be treated as classical (*non-quantizing*).

The increase of the atomic binding energies in the strong magnetic field tends to lower the ionization degree, as first guessed by Cohen, Lodenquai, & Ruderman (1970). Hence, there can be a significant amount of bound species in a highly magnetized atmosphere, even if it were negligibly small at the same temperature in the zero-field case. This idea has recently been confirmed by detailed NS atmosphere models (Rajagopal, Romani, & Miller 1997; Potekhin, Chabrier, & Shibanov 1999b; Potekhin & Chabrier 2003).

The effects of magnetic fields on the kinetic properties of the outer NS layers have been reviewed by, e.g., Yakovlev & Kaminker (1994) and Ventura & Potekhin (2001). A strongly quantizing magnetic field reduces the mean radiative opacities (see, e.g., Silant'ev & Yakovlev 1980); therefore, the bottom of the photosphere shifts to higher densities (see, e.g., Pavlov et al. 1995; Lai & Salpeter 1997).

A nonquantizing magnetic field does not affect thermodynamic functions of the plasma. However, it does affect the electron heat conduction, unless the *magnetization parameter*,

$$\omega_g \tau \approx 1760 \frac{B_{12}}{\sqrt{1+x_r^2}} \frac{\tau}{10^{-16} \text{ s}} , \quad (3)$$

is small. Here, $\omega_g = \omega_c / (1+x_r^2)^{1/2}$ is the electron gyrofrequency,

$$x_r = \hbar(3\pi^2 n_e)^{1/3} / (m_e c) \approx 1.0088 (\rho_6 Z / A)^{1/3} \quad (4)$$

is the *relativity parameter*, $\rho_6 \equiv \rho / (10^6 \text{ g cm}^{-3})$, and τ is an effective relaxation time. In a degenerate Coulomb plasma

with a nonquantizing magnetic field,

$$\tau \approx \frac{3\pi\hbar^3}{4Zm_e e^4 \Lambda \sqrt{1+x_r^2}} = \frac{5.700 \times 10^{-17}}{Z\Lambda \sqrt{1+x_r^2}} \text{ s}, \quad (5)$$

where Λ is an effective Coulomb logarithm. One has $\Lambda \sim 1$ in the ion liquid, and Λ is roughly proportional to T in the classical Coulomb solid (see, e.g., Yakovlev & Urpin 1980). However, according to Baiko et al. (1998), the correlation effects smooth the dependence of Λ on T or ρ near the melting point and introduce deviations from this proportionality.

In a magnetic field, one should generally introduce two different relaxation times (τ_{\parallel} and τ_{\perp}), determined by two Coulomb logarithms (Λ_{\parallel} and Λ_{\perp}), corresponding to electron transport parallel and perpendicular to the field lines. Analytic fits for Λ_{\parallel} and Λ_{\perp} at any B have been constructed by Potekhin (1999).

As seen from equations (3) and (5), the magnetization parameter is large in the outer NS envelope at $B \gtrsim 10^{11}$ G, typical for many isolated NSs. Moreover, according to equations (1) and (2), the magnetic field can be strongly quantizing in the outermost part of the envelope. Therefore, the field can greatly affect the heat conduction and the thermal structure of the NS envelope. In this case, the surface temperature T_s may be nonuniform, depending on the magnetic field geometry. Then, we introduce the effective temperature of the star T_{eff} , defined by

$$4\pi\sigma R^2 T_{\text{eff}}^4 = L_{\gamma} = \int F d\Sigma = \sigma \int T_s^4 d\Sigma, \quad (6)$$

where R is the stellar (circumferential) radius and $d\Sigma$ is the surface element. The quantities T_s , T_{eff} , and L_{γ} refer to a local reference frame at the NS surface. The redshifted (“apparent”) quantities as detected by a distant observer are $T_s^{\infty} = T_s(1-r_g/R)^{1/2}$, $T_{\text{eff}}^{\infty} = T_{\text{eff}}(1-r_g/R)^{1/2}$, and $L_{\gamma}^{\infty} = (1-r_g/R)L_{\gamma}$ (Thorne 1977), where $r_g = 2GM/c^2 = 2.95(M/M_{\odot})$ km is the Schwarzschild radius defined by the total gravitational NS mass M and G is the gravitational constant.

3. PHYSICS INPUT

Much of the physics input used in our work is the same as in Papers I and II. We outline these cases and refer the reader to Papers I and II for details.

3.1. Basic Equations

We choose the boundary between the internal NS region and the heat-blanketing envelope at the neutron drip density $\rho_b = 4 \times 10^{11}$ g cm $^{-3}$ (at a radius R_b a few hundred meters under the surface). Although $\rho_b = 10^{10}$ g cm $^{-3}$, adopted by Gudmundsson et al. (1983), ensures the necessary condition $R - R_b \ll R$ with higher accuracy, the present choice better conforms to the requirement that T does not vary over the boundary if a strong magnetic field is present (Paper II). In addition, we show that this choice provides a better accuracy to the T_b - T_s relation in the presence of an accreted envelope. On the other hand, the increase of ρ_b increases the thermal relaxation time of the blanketing envelope, thus hampering a study of rapid variability of the thermal emission (over timescales $\lesssim 10$ yr for $\rho_b \sim 4 \times 10^{11}$ g cm $^{-3}$; Ushomirsky & Rutledge 2001) with a cooling code.

The thermal structure of the blanketing envelope is studied in the stationary, local, plane-parallel approximation, assuming that a scale of temperature variation over the surface is much larger than the thickness of the blanketing envelope. This leads to the *one-dimensional* approximation for the heat diffusion equation:

$$F = \kappa \frac{dT}{dz}, \quad \kappa \equiv \frac{16\sigma T^3}{3K\rho}, \quad (7)$$

where κ is an effective thermal conductivity along the normal to the surface, K is the mean opacity, and $z = (R-r)(1-r_g/R)^{-1/2} \ll R$ is the local proper depth in the envelope.

Equation (7) can be reduced (see, e.g., Van Riper 1988) to

$$\frac{d \log T}{d \log P} = \frac{3}{16} \frac{PK}{g} \frac{T_s^4}{T^4}, \quad (8)$$

where P is the pressure. We integrate equation (8) inward from the radiative surface, where $T = T_s$, using the same algorithm as in Paper I. We place the radiative surface at the Rosseland optical depth equal to $\frac{2}{3}$.⁵ Another boundary condition would imply another integration constant for the integral of equation (8), which becomes negligible in the inner part of the envelope, where $T \gg T_s$ (see, e.g., Ventura & Potekhin 2001). Therefore, the choice of the boundary condition does not noticeably affect the heat flux and the T_b - T_s relation.

The validity of the one-dimensional approximation can be checked by two-dimensional simulation of the heat transport in the blanketing envelope. Such a simulation was attempted by Schaaf (1990b) for a homogeneously magnetized NS, under many simplified assumptions. The heat conduction from hotter to cooler zones along the surface or possible meridional and convective motions can smooth the temperature variations over the NS surface. Nevertheless, the one-dimensional approximation seems to be sufficient to simulate NS cooling.

The thermal conductivity tensor of a magnetized plasma is anisotropic. It is characterized by the conductivities parallel (κ_{\parallel}) and perpendicular (κ_{\perp}) to the field and by the off-diagonal (Hall) component. In the plane-parallel approximation, equation (7) contains the effective thermal conductivity,

$$\kappa = \kappa_{\parallel} \cos^2 \theta + \kappa_{\perp} \sin^2 \theta. \quad (9)$$

Assuming the dipole field, we use the general relativistic formulas

$$B(\chi) = B_p \sqrt{\cos^2 \chi + a^2 \sin^2 \chi}, \quad (10a)$$

$$\tan \theta = a \tan \chi, \quad (10b)$$

$$a = -\frac{(1-x) \ln(1-x) + x - 0.5x^2}{[\ln(1-x) + x + 0.5x^2] \sqrt{1-x}} \quad (10c)$$

(Ginzburg & Ozernoy 1964), where B_p is the field strength at the magnetic pole, χ is the polar angle, and $x = r_g/R$.

⁵ Assuming the local thermodynamic equilibrium, this depth follows from the Milne-Eddington formula, which is fairly accurate, as shown by Kourganoff (1948).

3.2. Equation of State

A nonaccreted heat-blanketing envelope is assumed to be composed of iron, which can be partially ionized at $\rho \lesssim 10^6 \text{ g cm}^{-3}$. Ions in the envelope form either Coulomb liquid or Coulomb crystal. The melting of the crystal occurs at $\Gamma = \Gamma_m \approx 175$ (see, e.g., Potekhin & Chabrier 2000), where $\Gamma = (Ze)^2/k_B T a_i$ is the ion coupling parameter, $a_i = (4\pi n_i/3)^{-1/3}$ is the ion sphere radius, and n_i is the ion number density. The melting curve $\Gamma = \Gamma_m$ is shown in Figure 1 as the dotted line. The figure demonstrates the thermal structure of a nonmagnetic iron envelope. The value of the surface gravity, $g = 2.43 \times 10^{14} \text{ cm s}^{-2}$, chosen in this example corresponds to the “canonical” NS model with $M = 1.4 M_\odot$ and $R = 10 \text{ km}$. At $B = 0$, as in Paper I, we use the OPAL EOS (Rogers, Swenson, & Iglesias 1996), extrapolated beyond the available tables using an effective charge number Z_{eff} . In the strong magnetic field, we employ the finite-temperature Thomas-Fermi EOS of Thorolfsson et al. (1998),⁶ with Z_{eff} evaluated as in Paper II.

As in Paper I, the accreted envelope is modeled by a sequence of layers of H, He, C, O, and Fe, and Fe is considered as the end point of nuclear transformations in the heat-blanketing envelopes. An example of the thermal

⁶ Available at <http://www.raunvis.hi.is/~ath/TFBT>.

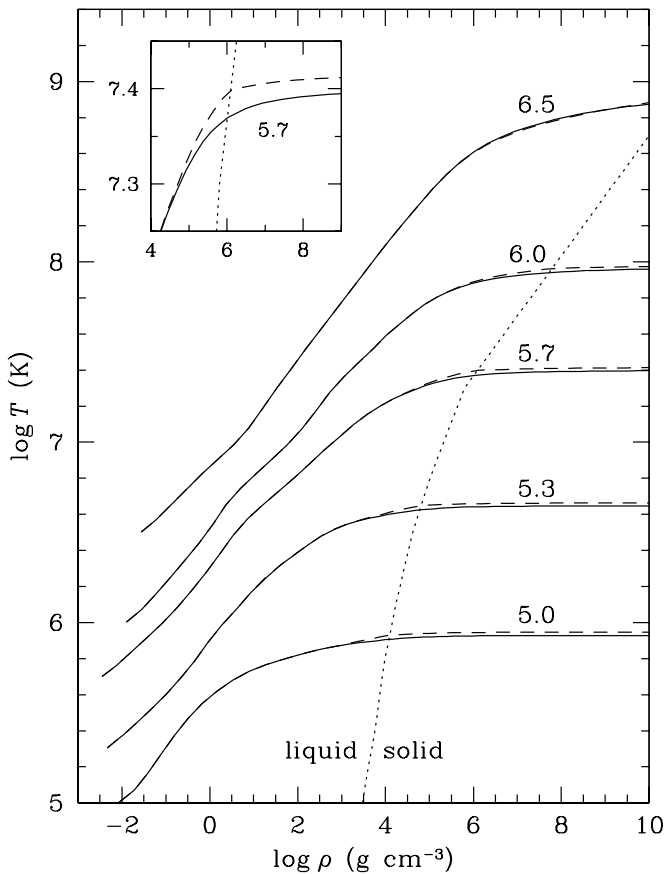


FIG. 1.—Temperature profiles in a nonaccreted, nonmagnetized envelope of a canonical NS ($M = 1.4 M_\odot$, $R = 10 \text{ km}$) for several values of T_s (marked by $\log T_s$). *Solid lines*: Calculation with the improved electron conductivities; *dashed lines*: from Paper I. The dotted line shows the liquid/solid boundary. Inset shows a temperature profile near this boundary in more detail.

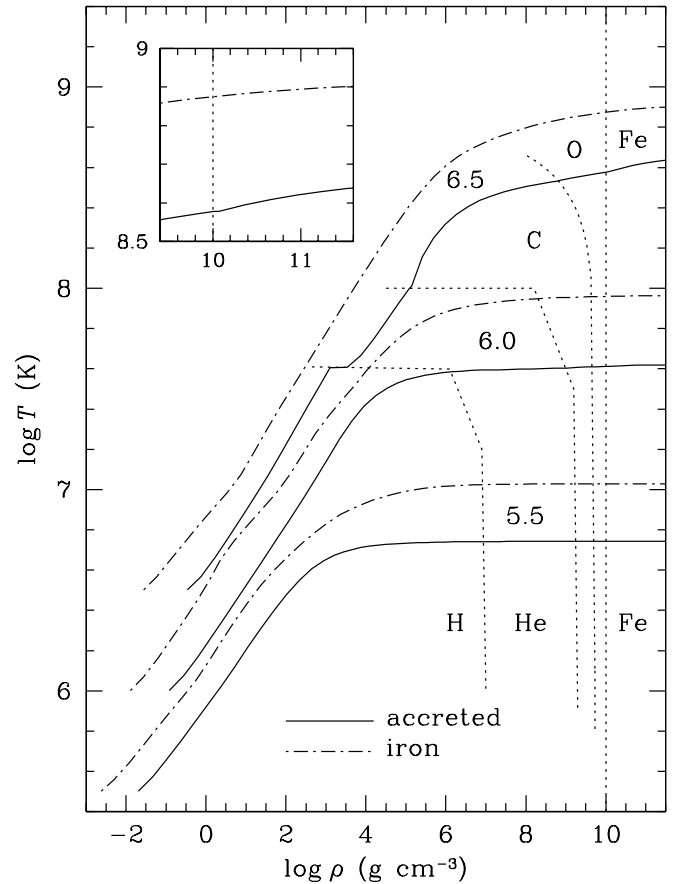


FIG. 2.—Temperature profiles in a nonmagnetized envelope of a canonical NS containing maximum accreted mass (*solid lines*), compared with the iron envelope (*dot-dashed lines*). The dotted lines correspond to interfaces between the layers of different chemical elements. The inset demonstrates the temperature increase in the hot envelope behind the deepest accreted layer.

structure of a nonmagnetic accreted envelope is shown in Figure 2. The boundaries between the layers are determined by the conditions of thermo- and pycnonuclear burning of the selected elements and by ΔM , the mass of light elements (from H to O). These approximate boundaries are shown in Figure 2 as dotted lines. In that example, the envelope is *fully accreted*: light elements reach the density $\sim 10^{10} \text{ g cm}^{-3}$, where pycnonuclear burning of oxygen becomes efficient. Compared to Paper I, we have improved the position of the C/O boundary, taking into account the results of Sahrting & Chabrier (1998). Their carbon ignition curve is approximately reproduced by the formula

$$T \approx \frac{5.2 \times 10^8 \text{ K}}{\{1 + [0.2 \ln(\rho_{\text{pyc}}/\rho)]^{-0.7}\}^{0.07}} \quad (11)$$

at $\rho < \rho_{\text{pyc}} \approx 5.5 \times 10^9 \text{ g cm}^{-3}$. The latter improvement, however, has almost no effect on T_s .

As demonstrated recently by Schatz et al. (2001), an explosive or steady state burning of hydrogen in the surface layers of accreting NSs may be strongly affected by the rapid proton (rp) capture process and extend to elements like Sn, Sb, and Te, much heavier than Fe. We do not consider this possibility here but intend to analyze it in a separate publication.

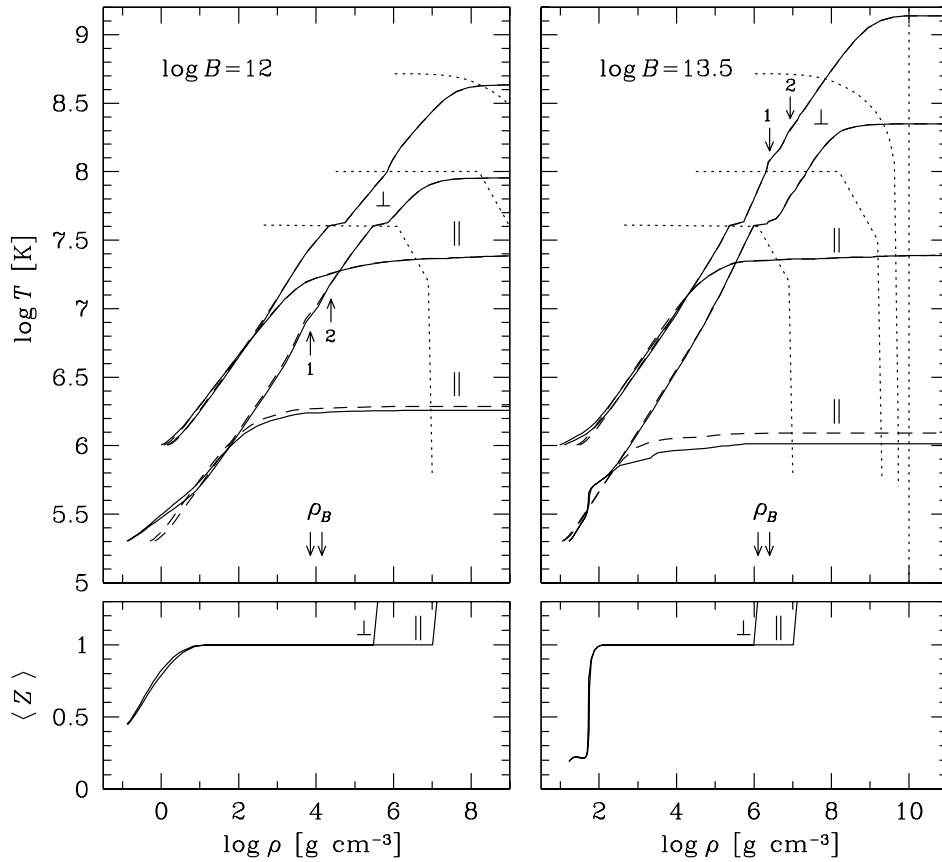


FIG. 3.—Temperature profiles (*top panels*) in the accreted envelope ($\Delta M/M = 1.5 \times 10^{-7}$) of the canonical NS with $B = 10^{12}$ G (*left*) and $10^{13.5}$ G (*right*), for $T_s = 2 \times 10^5$ K (the curves that start in the atmosphere at lower T) and 10^6 K. At each T_s , the lower curve corresponds to the radial magnetic field ($\theta = 0$; *parallel sign*) and the upper to the tangential one ($\theta = 90^\circ$; *perpendicular sign*). The solid lines are obtained using the hydrogen EOS and the opacities of Potekhin & Chabrier (2003) for the partially ionized atmosphere; the corresponding mean ion charge number is plotted in the bottom panels. The dashed profiles are calculated using the EOS of fully ionized ideal gas. The two arrows marked “ ρ_B ” indicate the density below which the field is strongly quantizing for hydrogen or helium (*left- and right-hand arrows, respectively*). The arrows marked “1” and “2” indicate filling of the first and the second electron Landau levels, respectively [ρ_B and $(2 + \sqrt{2})\rho_B$, calculated for H in the left-hand and for ^{12}C in the right-hand panel].

The outermost accreted layer is assumed to consist of hydrogen. Even a hydrogen atmosphere of a “warm” NS can be partially ionized in a strong magnetic field. Therefore, we use the EOS of partially ionized hydrogen in strong fields, derived by Potekhin et al. (1999b) and tabulated by Potekhin & Chabrier (2003) at $11.9 < \log_{10} B < 13.5$ (where B is in gauss). Beyond the tabulated range, we employ the model of a fully ionized ideal electron-ion plasma. As demonstrated below (Fig. 3), the inaccuracy introduced by the latter approximation can be significant for cold NSs ($T_b < 10^7$ K) with superstrong magnetic fields ($B > 10^{13.5}$ G). The fully ionized ideal electron-ion plasma model is also used for He, C, and O, which occupy deeper layers.

3.3. Opacities

Heat is carried through the NS envelope mainly by electrons at relatively high densities and by photons near the surface. Hence,

$$\kappa = \kappa_r + \kappa_e, \quad K^{-1} = K_r^{-1} + K_e^{-1}, \quad (12)$$

where κ_r , κ_e and K_r , K_e denote the radiative (r) and electron (e) components, respectively, of the thermal conductivity κ and opacity K .

Typically, the radiative conduction dominates ($\kappa_r > \kappa_e$) in the outermost, nondegenerate NS layers,

whereas the electron conduction dominates ($\kappa_e > \kappa_r$) in deeper, moderately or strongly degenerate layers. We see below, however, that in the superstrong magnetic fields the radiative conduction can be important up to higher densities. The T_b - T_s relation mostly depends on the conductivities in the *sensitivity strip* on the ρ - T plane (Gudmundsson et al. 1983), where $\kappa_e \sim \kappa_r$. The $T(\rho)$ profiles flatten in the inner NS zone beyond this strip (e.g., see Figs. 1 and 2).

Following Paper II, we use the updated electron conductivities, κ_e , presented by Potekhin et al. (1999a) for $B = 0$ and Potekhin (1999) for $B \neq 0$.⁷ Unlike the previous expressions for κ_e , the updated results take into account multiphonon absorption and emission processes in Coulomb crystals and incipient long-range order in strongly coupled Coulomb liquids of ions. As argued by Baiko et al. (1998), these processes are important near the melting, $0.3\Gamma_m \lesssim \Gamma \lesssim 3\Gamma_m$, and they almost remove the jump of κ_e at the liquid-solid interface.

The effect of the conductivity update on the thermal structure at $B = 0$ is illustrated by Figure 1. It is marginally significant at low T_b and insignificant at $T_b \gtrsim 10^8$ K.

⁷ Available at <http://www.ioffe.ru/astro/conduct>.

The inset in Figure 2 zooms in on the innermost parts of the upper (hottest) profiles for the nonaccreted and accreted envelopes. For the accreted envelope, the profile noticeably mounts at $\rho > 10^{10} \text{ g cm}^{-3}$, because the crossing of the O/Fe interface is accompanied by a decrease of κ_e due to the jump of Z . The decrease of κ_e has a smaller effect on the temperature profiles at lower T .

Radiative opacities of hydrogen at moderately strong magnetic field are taken from Potekhin & Chabrier (2003). These opacities are contributed by free-free, bound-free, and bound-bound transitions and electron scattering. They are calculated taking into account detailed ionization balance in strong magnetic fields. Figure 3 shows the thermal structure of accreted NS envelopes at two values of T_s and two values of B for the magnetic fields radial and tangential to the NS surface. Solid lines are obtained using the EOS and opacities of Potekhin & Chabrier (2003), while dashed lines correspond to the ideal fully ionized plasma model. At $T_s = 10^6 \text{ K}$ the latter model appears to be satisfactory, whereas at lower T_s there are appreciable differences.

The difference at the lowest densities (in the atmosphere) is produced by the contribution of bound species (atoms) in the EOS and opacities. The bottom panels of Figure 3 show the mean ion charge $\langle Z \rangle$ along the lower ($T_s = 2 \times 10^5 \text{ K}$) profiles, confirming that $\langle Z \rangle$ is considerably smaller than 1 in the atmosphere. At this relatively low temperature, the ionization proceeds smoothly for $B = 10^{12} \text{ G}$, but rather sharply (via pressure ionization) for $B = 10^{13.5} \text{ G}$. Simultaneously with the pressure ionization, the temperature climbs steeply along the profiles in the top right-hand panel, because a sharp increase of P (due to the increasing number of free particles) contributes to the right-hand side of equation (8).

The difference between the ideal gas (*dashed line*) and accurate (*solid line*) profiles at higher (subphotospheric) densities arises from the Coulomb interaction. This interaction gives a negative contribution to P , thus decreasing the right-hand side of equation (8).

We adopt the same radiative opacities of iron as in Papers I and II for zero and strong B , respectively. In the first case, we use the OPAL opacities (Iglesias & Rogers 1996). For strong B , we use the free-free and scattering opacity fits from Paper II. However, in the present paper (as in Paper I and in Potekhin & Chabrier 2003) we assume that radiation does not propagate at frequencies below the electron plasma frequency, $\omega_{\text{pl}} = (4\pi e^2 n_e / m_e)^{1/2}$; thus, we cut off the integration over photon frequencies ω in the Rosseland mean opacities at $\omega < \omega_{\text{pl}}$. We found that, under this assumption, the fit expressions for K_r given in Paper II should be multiplied by a correction factor of $\approx \exp\{0.005[\ln(1 + 1.5\hbar\omega_{\text{pl}}/k_B T)]^6\}$, which effectively eliminates the radiative transport at large densities, where $\hbar\omega_{\text{pl}} \approx 28.8 \text{ keV}(\rho_6 Z/A)^{1/2} \gg k_B T$.

For He, C, and O, we also employ the opacity fits from Paper II, with the above plasma frequency correction. The effect of this correction on the thermal structure of the accreted envelope is illustrated in Figure 4. It is unimportant at moderately strong magnetic fields, but quite significant at superstrong fields, because of the high photosphere densities in the latter case. The effect becomes less pronounced at higher T_s . Actually, some plasma waves can propagate at $\omega < \omega_{\text{pl}}$ (see, e.g., Ginzburg 1970) and carry the heat; thus, we expect that realistic temperature profiles should lie between the solid and dashed curves in Figure 4.

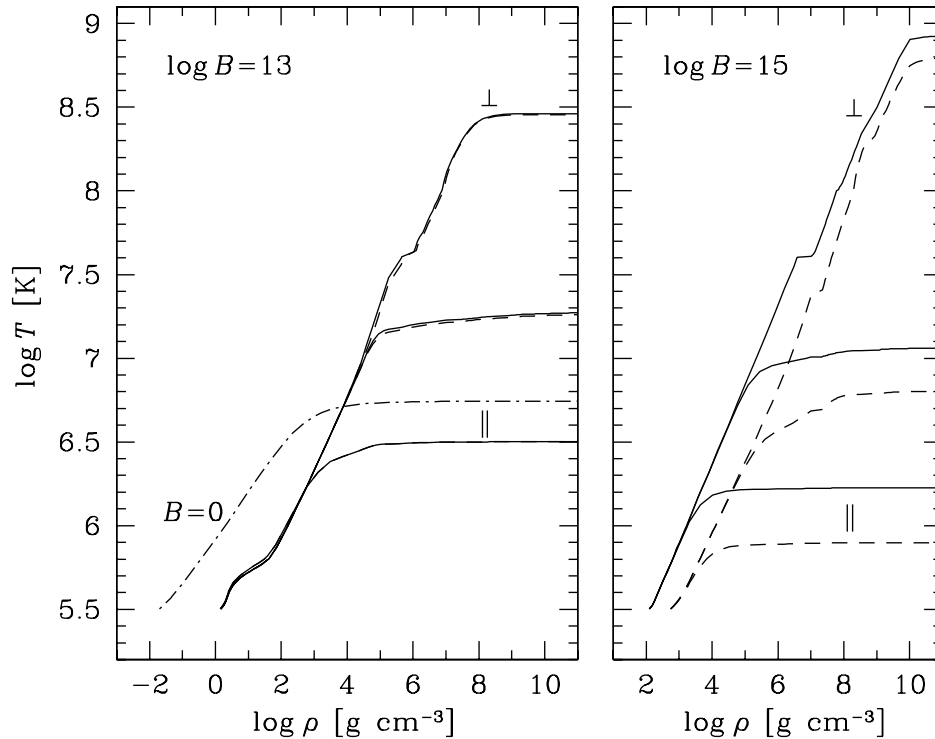


FIG. 4.—Temperature profiles in the accreted envelope for the same stellar parameters as in Fig. 3, but at $B = 10^{13} \text{ G}$ (left) and 10^{15} G (right), for $T_s = 10^{5.5} \text{ K}$, with (*solid lines*) and without (*dashed lines*) a plasma frequency cutoff, at $\theta = 0^\circ$ (bottom lines), 84° (middle lines), and 90° (top lines). The dot-dashed line in the left-hand panel is for $B = 0$.

4. THERMAL STRUCTURE

4.1. Temperature Profiles

We integrated equation (8) for various magnetic field strengths B , inclination angles θ , surface temperatures T_s , and accreted masses ΔM , using the envelope models described in the previous section. We performed the calculations at two values of the surface gravity, $g = 10^{14}$ and $2.43 \times 10^{14} \text{ cm s}^{-2}$, and checked that the approximate scaling relation $T_s \propto g^{1/4}$, obtained by Gudmundsson et al. (1983) and confirmed in Papers I and II, also holds in the present case.

As is clear from the discussion in § 3, our EOS and opacity models may be crude at $B \gtrsim 10^{14} \text{ G}$. Further improvements of the physics input are required in superstrong fields.

Some examples of calculated temperature profiles at several values of T_s are shown in Figures 3 and 4, discussed above. Figure 5 displays the profiles at two values of B and three values of θ for $\Delta M = 2 \times 10^{-7} M_\odot$ (solid lines) and 0 (dot-dashed lines) and for two values of T_b (10^8 and 10^9 K).

4.2. Relation between Internal and Effective Temperatures

Using the above results, we have calculated the T_b - T_s relation for a number of input parameters. We confirm the conclusion of Paper I that the relation is rather insensitive to the details of the distribution of different chemical elements within the accreted envelope, but depends mainly on ΔM , the total mass of the elements from H to O. In particular, all hydrogen can be replaced by He, leaving the T_b - T_s relation almost unchanged.

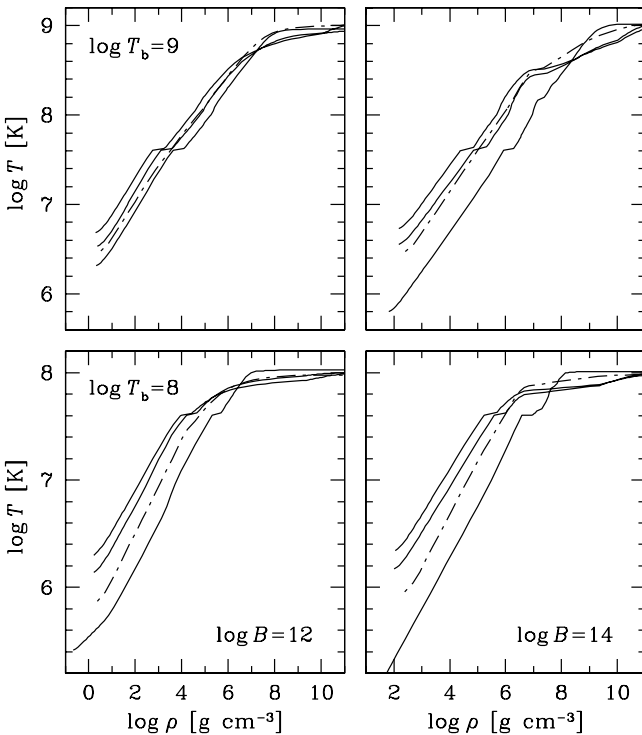


FIG. 5.—Temperature profiles in the accreted envelope for the same stellar parameters as in Fig. 3, but at $B = 10^{12} \text{ G}$ (left) and 10^{14} G (right), for $T_b = 10^8$ (bottom) and 10^9 K (top), at $\theta = 90^\circ, 84^\circ$, and 0° (from steepest to least steep lines). The dot-dashed lines correspond to iron envelopes at $\theta = 84^\circ$.

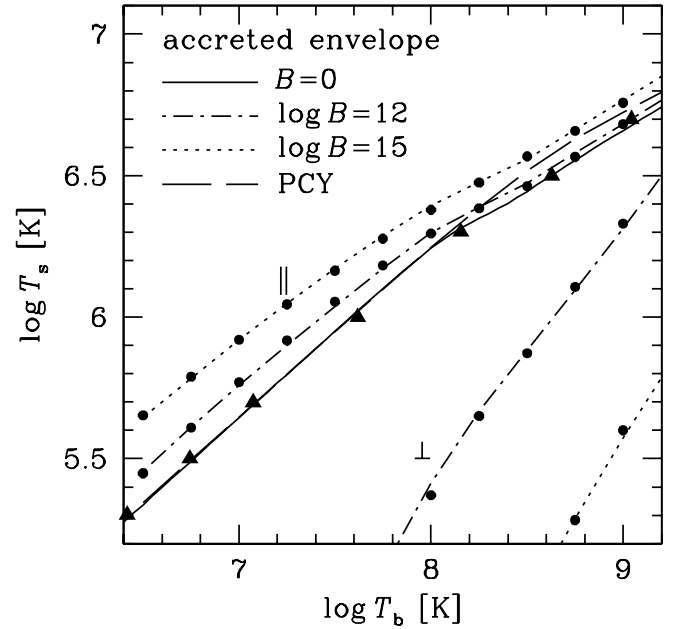


FIG. 6.— T_s vs. T_b for a canonical NS with a fully accreted envelope ($\Delta M = 2 \times 10^{-7} M_\odot$). Solid line: $B = 0$; dot-dashed line: $B = 10^{12} \text{ G}$; dotted line: $B = 10^{15} \text{ G}$; dashed line: approximation from Paper I ($B = 0$). Circles and triangles show the numerical results. At $B \neq 0$, the lower lines correspond to $\theta = 90^\circ$ (perpendicular sign) and upper lines to $\theta = 0^\circ$ (parallel sign).

We have compared our T_b - T_s relation with that calculated by Brown et al. (2002; their Fig. 4) for nonmagnetized accreted envelopes composed of H, He, and Fe. The agreement is quite satisfactory.

We have fitted our numerical T_b - T_s relation calculated for magnetized accreted envelopes with analytic formulas (presented in the Appendix). In the limits of $B = 0$ and/or $\Delta M = 0$, these formulas do not exactly reproduce the fits obtained in Papers I and II. The differences reflect the improvements in the physics input and envelope models discussed in § 3. For instance, in calculations shown in Figure 5, the boundary condition for the integration inside the star was determined using the fitting formulas for T_s presented in the Appendix. The good convergence of the profiles toward the desired T_b confirms the accuracy of our fits.

Figure 6 illustrates the T_b - T_s relation for the fully accreted envelope of the canonical NS without a magnetic field, with a moderately strong field $B = 10^{12} \text{ G}$, and with a superstrong field $B = 10^{15} \text{ G}$, for two field geometries—normal ($\theta = 0^\circ$) and tangential ($\theta = 90^\circ$) to the surface. The lines show the fit, and the symbols (circles and triangles) show the numerical results. The nonmagnetic fit of Paper I is plotted as the dashed line. Its deviation from the present results (solid line) at high temperatures is mainly explained by the change of ρ_b (§ 3.1).

Figure 7 illustrates the T_b - T_s relation for the canonical NS with fully, partly, and nonaccreted envelopes at $\theta = 0^\circ$ and 90° . The longitudinal heat transport ($\theta = 0^\circ$) is enhanced by the accreted envelope and/or the strong magnetic field, thus increasing T_s . However, the transverse transport (lower lines), which is reduced by the strong magnetic field, is additionally reduced by the accreted envelope, further decreasing T_s . Actually, in longitudinal and transverse cases the lowering of Z increases the effective electron

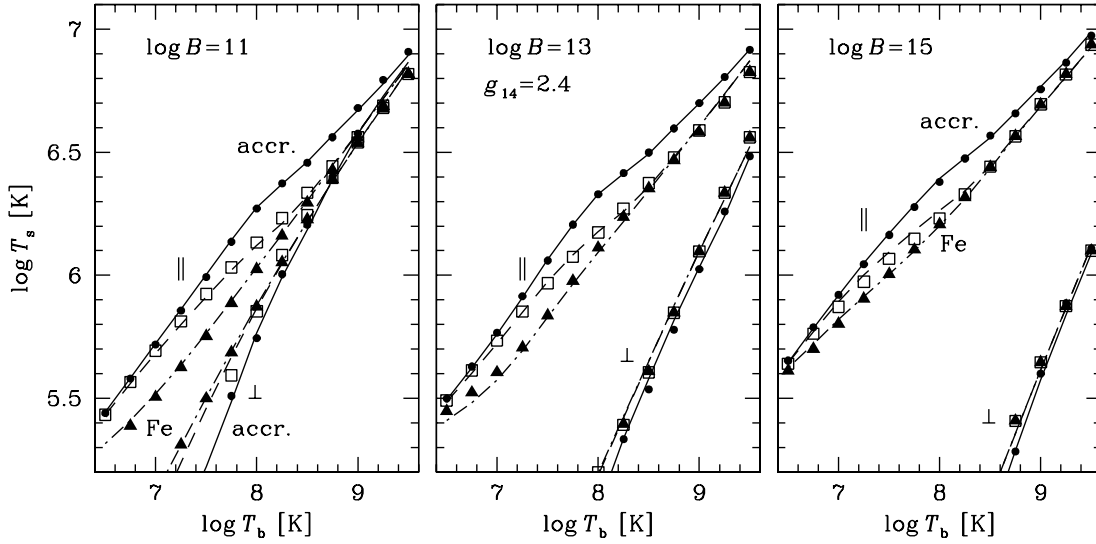


FIG. 7.— T_s vs. T_b for a canonical NS with fully accreted envelope (solid lines), iron envelope (dot-dashed lines), and partly accreted envelope at $\Delta M/M = 10^{-12}$ (dashed lines), for $\theta = 0^\circ$ (upper lines) and $\theta = 90^\circ$ (lower lines). The lines show the fit, and the symbols show the numerical results, for $B = 10^{11}$ (left), 10^{13} (middle), and 10^{15} G (right).

relaxation time τ . However, at $\omega_g \tau \gg 1$, the transverse electron conductivity (contrary to the longitudinal conductivity or the conductivity at $B = 0$) is *inversely* proportional to τ (see, e.g., Yakovlev & Kaminker 1994; Potekhin 1999).

4.3. Total Photon Luminosities

In order to calculate the cooling curves, one needs the total photon luminosity L_γ as a function of T_b . In the magnetic case, L_γ is given by the average over the surface, equation (6).

Figure 8 displays the photon luminosity versus B for two selected values of T_b (3×10^7 and 3×10^8 K) and four selected values of ΔM . The dependence of L_γ on B is com-

plicated. At $T_b = 3 \times 10^8$ K (in a warm NS) and with not very strong fields, the equatorial reduction of the heat transport clearly dominates, and the NS luminosity is lower than at $B = 0$. For higher B , the polar enhancement of the heat transport becomes more important, and the magnetic field increases the photon luminosity. At $T_b = 3 \times 10^7$ K (in a much colder NS), the effect of magnetic fields $B \lesssim 10^{13}$ G is very weak, while the increase of L_γ by stronger fields is much more pronounced. This is because the electron contribution into conduction becomes lower (and the radiative contribution higher) in a cold plasma. Accordingly, the equatorial decrease of the heat transport (associated with electron conduction) is weaker. On the other hand, the quantum effects increase both the electron and radiative thermal conductivities and are more pronounced in a colder plasma. Generally, the photon luminosity is not a simple function of B , because it is affected by a number of factors. Radiative opacities, longitudinal electron conductivities, and the position of the radiative surface all depend on B and affect T_s . In Figure 8, the variation of L_γ for $B_p < 10^{14}$ G does not exceed a factor of 2.5.

A higher B causes a more significant increase of the photon luminosity. However, in this case the effect of an accreted envelope is weaker than at $B = 0$. The origin of this weakening is explained in Figure 9, which illustrates the dependence of the local effective temperature on the magnetic latitude, specified by the polar angle χ (eq. [10b]), for a canonical NS with $T_b = 2 \times 10^8$ K. The dashed and solid lines refer to the nonaccreted and fully accreted envelopes, respectively. The horizontal lines refer to the case of $B = 0$, in which the accreted envelope increases T_{eff} by a factor of 1.73. The curved lines show the case of $B_p = 10^{15}$ G. Since the effects of the magnetic field weaken with increasing temperature (Paper II), the increase of T_s at the magnetic pole for the hotter accreted envelope is smaller than the analogous increase for the cooler iron envelope. Hence, the equatorial band, where T_s decreases, is broader for the accreted envelope, leading to an additional compensation of the total luminosity increase.

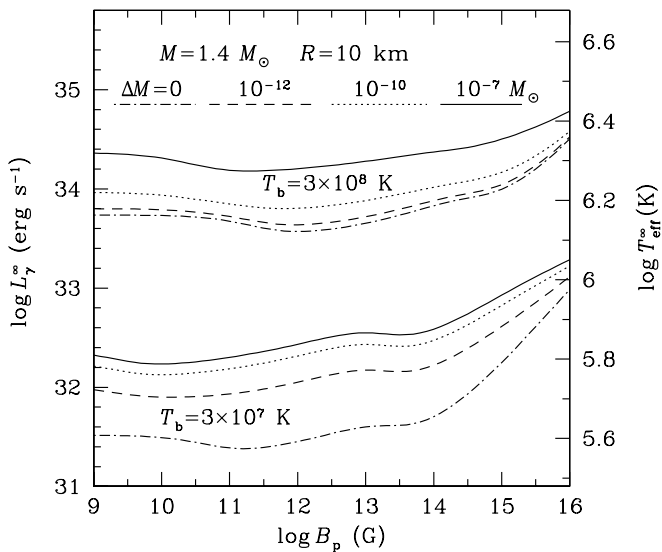


FIG. 8.—Photon surface luminosity (redshifted as detected by a distant observer: left-hand axis; redshifted effective surface temperature: right-hand axis) of a canonical NS with a dipole magnetic field, for two values of T_b and four models of the heat-blanketing envelope (accreted mass $\Delta M = 0$, 10^{-12} , 10^{-10} , or $10^{-7} M_\odot$) vs. magnetic field strength at the magnetic pole.

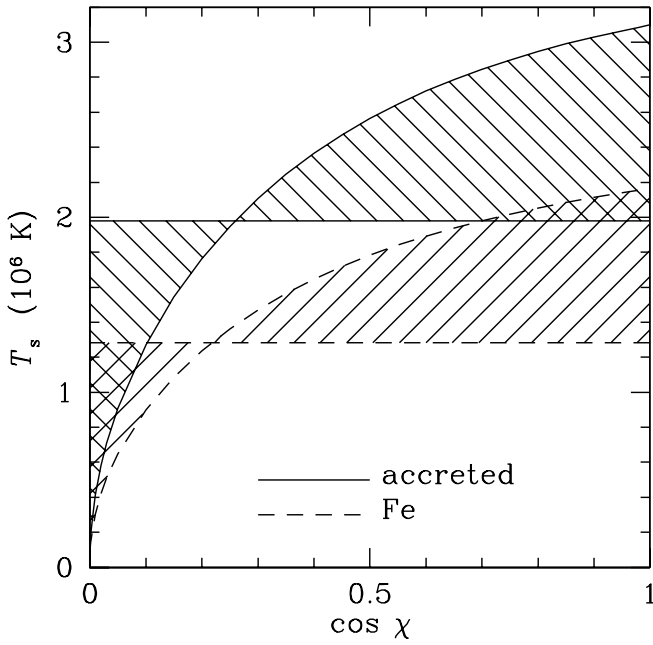


Fig. 9.—Local surface temperature (in units of 10^6 K) vs. cosine of the polar angle χ for an NS model with $M = 1.4 M_\odot$, $R = 10$ km, $T_b = 2 \times 10^8$ K, and $B = 0$ (horizontal lines) and the dipole field with $B_p = 10^{15}$ G (curves), for nonaccreted (dashed lines) and accreted (solid lines) envelopes.

5. COOLING

Let us outline the effects of accreted envelopes and surface magnetic fields on NS cooling. We use the same non-isothermal, general relativistic cooling code as in Gnedin et al. (2001), but incorporate the above effects of accreted envelopes and surface magnetic fields. In particular, we have shifted the inner boundary of the heat blanketing envelope to the neutron drip density (see § 3.1).

For simplicity, we assume that the NS cores are composed of neutrons, protons, and electrons. We adopt two model EOSs of this matter, EOS A and EOS B, based on the EOSs proposed by Prakash, Ainsworth, & Lattimer (1988) and described, for instance, in Yakovlev et al. (2002a). EOS A is model I of Prakash et al. (1988), with the compression modulus of saturated nuclear matter $K = 240$ MeV. EOS B corresponds to $K = 180$ MeV and to the simplified form of the symmetry energy proposed by Page & Applegate (1992). The NS models based on EOSs A and B are described, for instance, by Gnedin et al. (2001). EOS A is somewhat stiffer and yields a maximum NS mass of $1.98 M_\odot$, while EOS B yields a maximum mass of $1.73 M_\odot$. Both EOSs allow the powerful direct Urca process of neutrino emission to operate at sufficiently high densities, $\rho > \rho_D$ (with

$\rho_D = 7.85 \times 10^{14}$ and 1.298×10^{15} g cm $^{-3}$ for EOSs A and B, respectively). We consider NS models of two masses, 1.3 and $1.5 M_\odot$. The parameters of these models are listed in Table 1: ρ_c is the NS central density, M_{crust} the crust mass, ΔR_{crust} the crust thickness (defined as $\Delta R_{\text{crust}} = R - R_{\text{cc}}$, R_{cc} being the circumferential radius of the crust-core interface), M_D the mass of the inner core (if available) where the direct Urca process operates, and R_D the circumferential radius of this core. The central densities of the low-mass NSs, $1.3 M_\odot$, are smaller than ρ_D for both EOSs. They give an example of slow cooling. The central densities of $1.5 M_\odot$ NSs exceed ρ_D ; i.e., these models give us an example of fast cooling.

5.1. Overall Effects

Figure 10 shows the effects of the surface magnetic fields and accreted envelopes on the cooling of 1.3 (solid lines) and $1.5 M_\odot$ (dashed lines) nonsuperfluid NS models with EOS B in the core.

The left-hand panel of Figure 10 illustrates the effects of accreted envelopes in nonmagnetized NSs. We present the cooling curves for some values of ΔM , the mass of relatively light elements (H, He, C, and O) in the heat-blanketing envelopes. The curves for nonaccreted (Fe) envelopes are plotted as thick lines. The fraction of accreted mass $\Delta M/M$ varies from 0 (nonaccreted envelopes) to $\sim 10^{-7}$ (fully accreted envelopes); a further increase of ΔM is limited by the pycnonuclear burning of light elements (see Paper I).

During the first 50 yr after birth, 1.3 and $1.5 M_\odot$ NSs have nearly the same surface temperatures, since the surface is thermally decoupled from the stellar interiors (see, e.g., Gnedin et al. 2001). Later, after thermalization, the direct Urca process in the $1.5 M_\odot$ NS makes this NS much colder. The change of slopes of the cooling curves at $t \sim 10^5$ yr reflects the transition from the neutrino to the photon cooling stage. At the neutrino stage, the internal stellar temperature is ruled by the neutrino emission and is thus independent of the thermal insulation of the blanketing envelope. The surface photon emission is determined by the $T_b - T_{\text{eff}}$ relation. Since the accreted envelopes of not-too-cold NSs are more heat-transparent, the surface temperature of an accreted star is noticeably higher than that of a nonaccreted one. One can see that even a very small fraction of accreted matter, such as $\Delta M/M \sim 10^{-13}$, can change appreciably the thermal history of the star. The colder the star, the smaller the fraction of accreted material that yields the same cooling curve as the fully accreted blanketing envelope. This effect is more pronounced for the fast cooling.

At $t \gtrsim 10^5$ yr, a star enters the photon cooling stage. Since the accreted blanketing envelopes have lower thermal insulation, the NSs with such envelopes cool faster at the photon stage than the nonaccreted NSs (Fig. 10). Thus, the light elements have the opposite effects on the surface temperature

TABLE 1
NEUTRON STAR MODELS

EOS	M (M_\odot)	R (km)	ρ_c ($\times 10^{14}$ g cm $^{-3}$)	M_{crust} (M_\odot)	ΔR_{crust} (km)	M_D (M_\odot)	R_D (km)
A.....	1.3	13.04	7.44	0.057	1.58
	1.5	12.81	9.00	0.049	1.26	0.137	4.27
B.....	1.3	11.86	10.70	0.039	1.26
	1.5	11.38	14.20	0.028	0.93	0.065	2.84

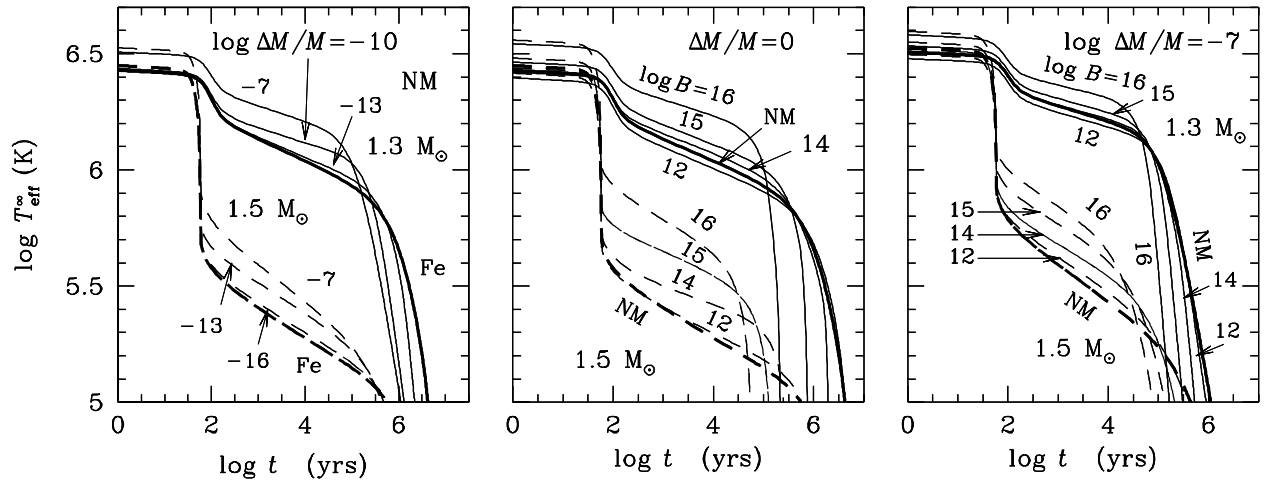


FIG. 10.—Cooling of nonsuperfluid NSs with $M = 1.3$ (slow neutrino emission; *solid lines*) and $1.5 M_{\odot}$ (fast neutrino emission; *dashed lines*), assuming EOS B in the NS cores. *Left*: Nonmagnetic (“NM”) NSs with differing amounts ΔM of light elements in the heat-blanketing envelopes [the values of $\log(\Delta M/M)$ are shown near the curves]; thick curves refer to nonaccreted (Fe) envelopes. *Middle*: Nonaccreted envelopes with dipole surface magnetic fields (the curves are marked with $\log B$, where $B = B_p$ is the field at the pole); thick lines refer to $B = 0$. *Right*: Same as the middle panel, but with a fully accreted envelope.

at the neutrino and photon cooling stages. This *reversal* of the effect when passing from one stage to the other is very well known and quite natural. Similar results have been obtained in Paper I, but our new $T_{\text{eff}}-T_b$ relation slightly weakens the effect of accreted envelopes.

The middle panel of Figure 10 displays the effect of dipole magnetic field on the cooling of NSs with nonaccreted envelopes. We present the cooling curves for several magnetic field strengths at the magnetic poles (numbers next to the curves) up to $B_p = 10^{16}$ G. The cooling curves of nonmagnetic NSs are plotted as thick lines. For simplicity, the magnetic field is treated as fixed (nonevolved). The thermal state of the stellar interior is almost independent of the magnetic field in the NS envelope at the neutrino cooling stage, but is affected by the magnetic field later, at the photon cooling stage. On the contrary, the surface temperature is always affected by the magnetic field.

The dipole field with $B_p \lesssim 10^{13}$ G makes the blanketing envelope of a warm ($1.3 M_{\odot}$) NS overall less heat-transparent (§ 4.3). This lowers T_{eff} at the neutrino cooling stage and slows down cooling at the photon cooling stage. The dipole field with $B_p \gg 10^{13}$ G makes the blanketing envelope overall more heat-transparent, increasing T_{eff} at the neutrino cooling stage and accelerating the cooling at the photon stage. The field with $B_p \sim 10^{13}$ G has almost no effect on the NS cooling. The presented results are in satisfactory agreement with those of our previous studies (Paper II).

The rapid cooling of colder magnetized ($1.5 M_{\odot}$) NSs is somewhat different. A strong magnetic field makes the heat-blanketing envelopes of these NSs overall more heat-transparent (§ 4.3), i.e., increases T_{eff} at the neutrino cooling stage and decreases it at the photon cooling stage. The fields with $B_p \lesssim 10^{13}$ G have almost no effect on T_{eff} . On the contrary, the effects of higher fields, $B_p \gtrsim 10^{13}$ G, are much stronger than for slowly cooling NSs.

The right-hand panel of Figure 10 presents the cooling curves of NSs with fully accreted envelopes and the same dipole magnetic fields as in the middle panel. For an NS with $B_p \lesssim 10^{15}$ G at the neutrino cooling stage, the effect of the accreted envelope is stronger than the effect of the

magnetic field. For higher B_p , the magnetic effect dominates; the accreted envelope produces a rather weak additional rise of T_{eff} .

The main outcome of these studies is that even ultrahigh magnetic fields cannot change the average surface temperatures of young and warm NSs as appreciably as an accreted envelope can, although the distribution of the local surface temperature over the surface of a magnetized NS can be strongly nonuniform.

5.2. Very Slowly Cooling Low-Mass NSs

As demonstrated recently by Yakovlev, Kaminker, & Gnedin (2001), Yakovlev et al. (2002a), and Kaminker et al. (2002), the effects of strong magnetic fields and accreted envelopes are especially important in low-mass NSs (where the direct Urca process is forbidden) with a strong proton superfluidity in their cores. Such a superfluidity [with typical values of proton critical temperature $T_{\text{cp}}(\rho) \gtrsim 5 \times 10^9$ K] fully suppresses the modified Urca process, which otherwise would be the main neutrino emission mechanism in low-mass NSs. The neutrino emission is then generated in the reactions of neutron-neutron scattering; it is not suppressed by a proton superfluidity and becomes dominant.

The low-mass NSs with strongly superfluid protons have thus very low neutrino luminosity and form a special class of *very slowly cooling stars*. Their models are useful to interpret the observations of the isolated NSs hottest for their ages. According to Yakovlev et al. (2001, 2002b) and Kaminker et al. (2002), there are two such NSs among several isolated NSs whose thermal radiation has been detected. One of them, RX J0822–43, is young, while the other, PSR B1055–52, is much older. The third possible candidate, RX J1856–3754, was moved (Yakovlev et al. 2002b) from the class of very slowly cooling NSs to the class of faster coolers after the revision of its age (Walter & Lattimer 2002). In this subsection, we focus on the interpretation of the observations of RX J0822–43 and PSR B1055–52, taking into account the effects of magnetic fields and accreted envelopes. The latter effects are less important for the interpretation of observations of colder isolated NSs

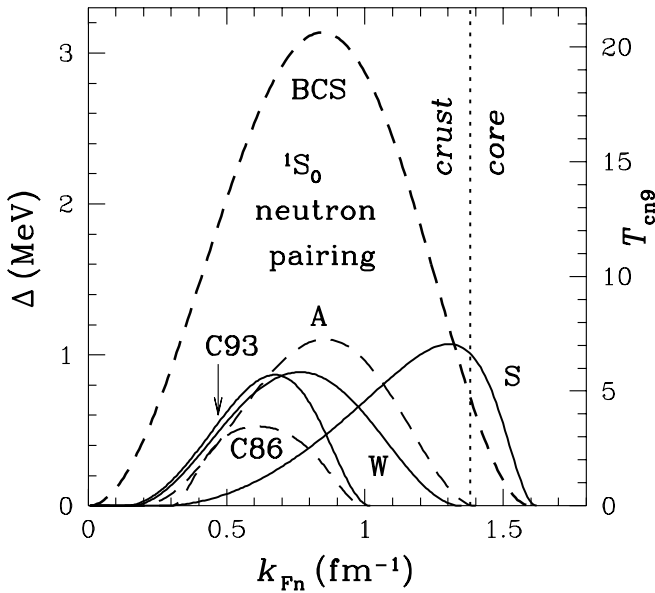


FIG. 11.—Energy gaps (left-hand axis) or critical temperature (right-hand axis) for various models of crustal neutron superfluidities (see text) vs. neutron Fermi wave number; the vertical line marks the crust-core interface.

(see, e.g., Kaminker et al. 2002 and Yakovlev et al. 2002a for a recent comparison of observations and cooling theories of NSs with nucleon cores).

Our analysis is illustrated in Figures 11 and 12. The observational limits $T_{\text{eff}}^{\infty} = 1.6\text{--}1.9$ MK (at the 90% confidence level) for RX J0822–43 (Fig. 12) are taken from Zavlin, Trümper, & Pavlov (1999). They are obtained by fitting the observed spectrum with the hydrogen atmosphere model; such a model is more appropriate for this source than the blackbody model of thermal emission. In contrast, it seems

more reasonable to fit the spectrum of PSR B1055–52 with a model containing a blackbody thermal component (see, e.g., Pavlov, Zavlin, & Sanwal 2002). The results of different groups are not fully consistent because of the complexity of observations and their interpretation. For instance, according to G. G. Pavlov (2002, private communication), the best-fit value obtained from the recent *Chandra* observations of PSR B1055–52 is $T_{\text{eff}}^{\infty} \approx 60$ eV. Attributing a typical error bar (at the 90% confidence level) derived from the observations of the same source somewhat earlier (G. G. Pavlov & M. Teter 2002, private communication), we have $T_{\text{eff}}^{\infty} = 60 \pm 6$ eV. An analysis of the recent *BeppoSAX* observations of PSR B1055–52 gives $T_{\text{eff}}^{\infty} = 75 \pm 6$ eV (Mineo et al. 2002) at the 68% confidence level. We adopt, somewhat arbitrarily, a wide T_{eff}^{∞} interval from 54 eV (the minimum value from the *Chandra* data) to 81 eV (the maximum value from the *BeppoSAX* data). We expect that this interval reflects the actual uncertainty of our knowledge of T_{eff}^{∞} for PSR B1055–52.

The NS ages are also known with some uncertainty. For RX J0822–43, we take the age range $t = 2\text{--}5$ kyr (as can be deduced, e.g., from a discussion in Arendt, Dwek, & Petre 1991) centered at $t = 3.7$ kyr (Winkler et al. 1988). For PSR B1055–52, we adopt the standard spin-down age of 530 kyr and assume that it is uncertain within a factor of 2.

For our analysis, we take a $1.3 M_{\odot}$ NS model with EOS A in the core. We use model 1p of sufficiently strong proton superfluidity in the core (in notations of Kaminker et al. 2002) and assume a weak (triplet-state) neutron pairing in the core, with the maximum critical temperature lower than 2×10^8 K. This weak neutron superfluidity has no effect on NS cooling and can be neglected in the cooling simulations. A stronger neutron superfluidity in the NS core would initiate a powerful neutrino emission due to Cooper pairing of neutrons accelerating NS cooling, in disagreement with the observations (see, e.g., Yakovlev et al. 2002a, 2002b). As shown by Yakovlev et al. (2001), the cooling of low-mass

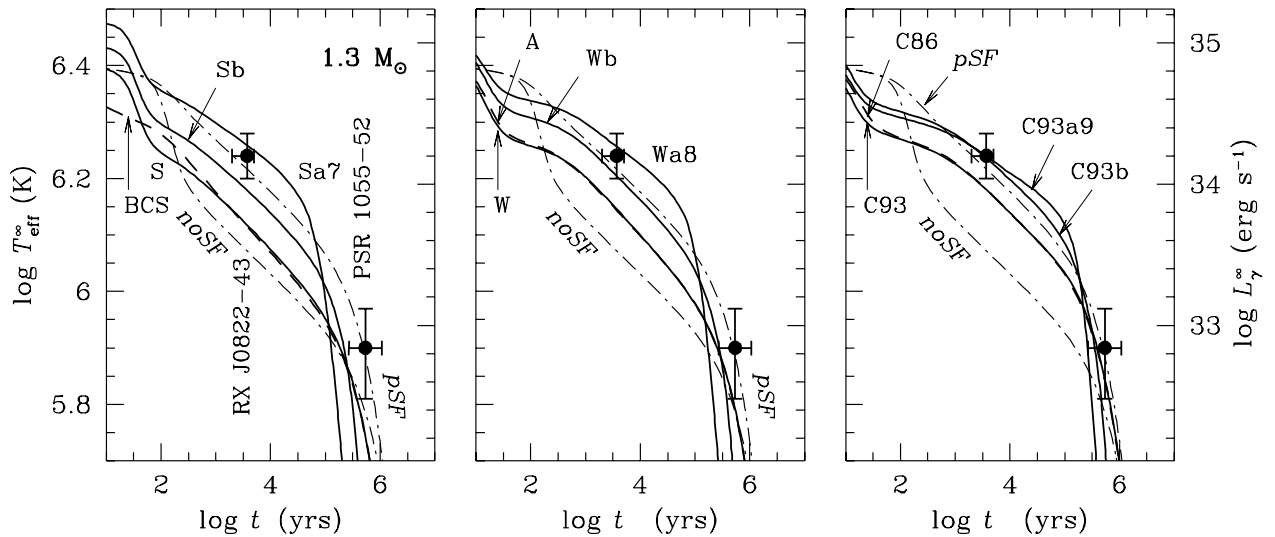


FIG. 12.—Evolution of redshifted effective surface temperature (T_{eff}^{∞}) or photon luminosity (L_{γ}^{∞}) of a low-mass ($1.3 M_{\odot}$) NS with EOS A confronted with observations of RX J0822–43 and PSR B1055–52. Dot-dashed curves are for a nonmagnetized, nonaccreted NS model without any superfluidity (“noSF”) or with a strong proton core superfluid alone (“pSF”). Other curves are obtained including the effects of proton core superfluidity and a model of crustal neutron pairing from Fig. 11 (“BCS” and “S” [left], “W” and “A” [middle], and “C86” and “C93” [right]). Models Sa7, Wa8, and C93a9 also include the effects of accreted envelopes with $\Delta M/M = 10^{-7}$, 10^{-8} , and 10^{-9} , respectively. Models Sb, Wb, and C93b refer to nonaccreted envelopes with dipole magnetic field $B_p = 10^{15}$ G.

NSs is rather insensitive to the model EOS in the NS core, the NS mass (as long as the mass is sufficiently low to avoid fast neutrino cooling in the NS core), and the model of proton superfluidity in the NS core [as long as the proton critical temperature is $\gtrsim (2-3) \times 10^9$ K over the core, to suppress the modified Urca process]. Therefore, model 1p of proton superfluidity is used just as an example, and the cooling curves are actually independent of the features of strong proton superfluidity. Let us add that it is likely that the cores of low-mass NSs consist of nucleons and electrons (with the direct Urca process forbidden). Muons may also be present there, but they have almost no effect on the cooling of low-mass NSs (Bejger, Yakovlev, & Gnedin 2003). Thus, our cooling scenarios are not related to the models of matter of essentially supranuclear density in the inner cores of massive NSs in which the composition may be exotic (e.g., including pion or kaon condensates or quark matter).

We see that the models of low-mass cooling NSs are sufficiently robust against uncertainties in the physics of matter in the NS cores. Accordingly, the cooling of this special class of NSs (contrary to the cooling of other NS models) is *especially sensitive to the properties of the NS crust*. It is mainly regulated by the effects of (1) accreted matter and (2) surface magnetic fields in the heat-blanketing envelopes, as well as by the effects of (3) singlet-state neutron superfluidity in the inner NS crusts. All these effects are of comparable strength. They are analyzed below and illustrated in Figures 11 and 12, with the aim of interpreting the observations of RX J0822–43 and PSR B1055–52.

Two dot-dashed curves marked “noSF” and “pSF” in each panel of Figure 12 show the cooling of a nonsuperfluid NS and an NS with strong proton superfluidity in the core (the effects of magnetic fields and accreted envelopes are neglected). We see that the proton superfluidity, indeed, delays the cooling (by suppressing the modified Urca process) and makes the cooling curves consistent with the observations of RX J0822–43 and PSR B1055–52 (Kaminker, Haensel, & Yakovlev 2001).

However, our “successful” pSF cooling curve neglects the presence of neutron superfluidity in the NS crust. This superfluidity is predicted by microscopic theories (see, e.g., Lombardo & Schulze 2001), although the superfluid gaps are very model-dependent. The superfluidity initiates neutrino emission due to Cooper pairing of crustal neutrons, which may noticeably accelerate the cooling of low-mass NSs (Yakovlev et al. 2001). In order to illustrate this effect, we consider several models of the crustal superfluidity. Figure 11 shows the dependence of the superfluid gap Δ (*left-hand axis*) or associated critical temperature T_{cn} (in units of 10^9 K; *right-hand axis*) on neutron Fermi wave number k_{Fn} (as a measure of density) for six models (from Lombardo & Schulze 2001). The vertical line indicates approximate position of the crust-core interface (assumed to be at 1.5×10^{14} g cm $^{-3}$ in our cooling models).

Model BCS is the basic model of singlet-state neutron pairing, calculated under the simplified assumption of purely in-vacuum neutron-neutron interaction (neglecting medium polarization effects). The other five models—C86 (Chen et al. 1986), C93 (Chen et al. 1993), A (Ainsworth, Wambach, & Pines 1989), W (Wambach, Ainsworth, & Pines 1993), and S (Schulze et al. 1996)—include medium polarization effects, which weaken the strength of neutron pairing.

In Figure 12, in addition to the noSF and pSF curves, we show six cooling curves (BCS, S, A, W, C86, and C93) calculated adopting proton superfluidity in the NS core and one of the models of neutron superfluidity in the crust from Figure 11 (neglecting surface magnetic fields and accreted envelopes). One can see that the crustal superfluidity indeed accelerates the cooling and complicates the interpretation of the observations of RX J0822–43 and PSR B1055–52. The six new curves are naturally divided into three pairs, shown in the three panels of Figure 12 (*left*: BCS and S; *middle*: A and W; *right*: C86 and C93). The curves within each pair are very close, while the pairs differ from one another. As is clear from Figure 11, the neutron superfluid gaps for any pair, although different, have one common property: the same maximum density of superfluidity disappearance. This maximum density limits the density of the outer NS layer, where the neutrino emission due to the singlet-state pairing of neutrons operates and accelerates the cooling. For instance, neutron superfluids BCS and S extend to higher densities (penetrate into the NS core); Cooper pairing neutrino emission is generated from an extended layer and produces the most dramatic effect: the cooling curves go much lower than the pSF curve, strongly violating the interpretation of RX J0822–43 and almost violating the interpretation of PSR B1055–52. Superfluids A and W die at lower ρ (at the crust-core interface), Cooper pairing neutrinos are emitted from a smaller volume, and the cooling curves go higher, closer to the pSF curve. They do not explain RX J0822–43, but seem to explain PSR B1055–52. Finally, superfluids C86 and C93 disappear even at lower ρ , far before the crust-core interface; the emission volume gets smaller, and the cooling curves shift even closer to the pSF curve, simplifying the interpretation of RX J0822–43 and easily explaining PSR B1055–52.

All NSs should have the same EOS and superfluids in their interiors but may have different magnetic fields and accreted envelopes. The effects of latter factors are also illustrated in Figure 12. As discussed above, the cooling histories of NSs with the superfluid model BCS are almost the same as with S, those with model A are the same as with W, and those with model C86 are the same as with C93. Therefore, we do not consider the effect of magnetic fields and accreted envelopes on the models C86, A, and BCS. Let us recall that magnetic fields and accreted envelopes have opposite effects on the thermal states of NSs at the neutrino and photon cooling stages. PSR B1055–52 is just passing from one cooling stage to the other and has no superstrong magnetic field. It is not expected to possess an extended accreted envelope. Thus, the effects of magnetic fields and accreted envelopes on the evolution of this pulsar are thought to be minor.

The superfluid model S (or BCS) without any magnetic field or accreted envelope is only marginally consistent with the observations of PSR B1055–52 (Fig. 12, *left-hand panel*). If, however, we accept this model, then we can explain RX J0822–43 by switching on the effects of the accreted envelopes or surface magnetic fields. Curve Sb in the left-hand panel of Figure 12 is calculated adopting proton superfluid in the NS core, superfluid S in the crust, and the dipole magnetic field with $B_p = 10^{15}$ G (the magnetar hypothesis). Curve Sa7 is obtained for the same crustal superfluid, but for $B = 0$ and $\Delta M/M = 10^{-7}$ of accreted material on the NS surface. We see that both curves, Sb and Sa7, are consistent with the observations of RX J0822–43. A magnetic field

slightly above $B_p = 10^{15}$ G would further improve the agreement of the theory and observations.

The next superfluid model W (or A) is acceptable to interpret the observations of PSR B1055–52 (Fig. 12, *middle panel*). We can adopt it and switch on the effects of the magnetic field or accreted envelope to interpret RX J0822–43. Curve Wb in the right-hand panel corresponds to the crustal superfluid W and the dipole magnetic field with $B_p = 10^{15}$ G. Curve Wa8 is calculated for the same crustal superfluid, $B = 0$, but for $\Delta M/M = 10^{-8}$. Both curves, Wb and Wa8, are seen to be consistent with the observations of RX J0822–43.

Finally, model C93 (or C86) of crustal superfluid is in reasonable agreement with the data on PSR B1055–52 (Fig. 12, *right-hand panel*). Adding the effect of the surface magnetic field ($B_p = 10^{15}$ G; curve C93b) or the accreted envelope ($\Delta M/M = 10^{-9}$; curve C93a9), we can easily explain the observations of RX J0822–43.

Thus, all the models of crustal superfluidity are currently consistent with the observations (although models BCS and S seem to be less likely for explaining PSR B1055–52). This is a consequence of wide observational error bars of T_{eff}^∞ for PSR B1055–52 (see above). We expect to constrain the models of crustal superfluidity after better determination of T_{eff}^∞ in the future observations of PSR B1055–52. Afterward, it will be possible to constrain the surface magnetic fields and the mass of the accreted envelope from the observations of RX J0822–43.

It is clear from Figures 10 and 12 that old and warm NSs like PSR B1055–52 cannot possess bulky accretion envelopes, which would operate as efficient coolers. This conclusion is in line with the observations of thermal radiation from old sources: their spectra are better fitted (see, e.g., Pavlov et al. 2002) with the blackbody model of thermal emission (suitable for nonaccreted matter) than with the hydrogen atmosphere models. This conclusion is also in line with theoretical studies of Chang & Bildsten (2003), who show that light elements can be burned in old ($t \gtrsim 10^5$ yr) and warm NSs by diffusive nuclear burning. In this connection, it would be interesting to construct the models of cooling NSs incorporating the effects of diffusive burning and associated thinning of the light-element envelopes in time. Cooling of magnetars is expected to be accompanied by magnetic field decay, which should also be taken into account in advanced cooling simulations.

6. CONCLUSIONS

We have studied the thermal structure of a heat-blanketing envelope of an NS with a strong magnetic field and arbitrary amount of light-element (accreted) material.

We have calculated and fitted by an analytic expression the relation between the NS internal and surface temperatures in a local element of the heat-blanketing envelope as a function of magnetic field strength and geometry, the mass of accreted material, and the surface gravity. We have performed numerical simulations of the cooling of NSs with dipole magnetic fields and accreted envelopes. We have considered slow and fast cooling regimes, but mainly focused on very slow cooling of low-mass NSs with strong proton superfluidity in their cores. These NSs form a special class of NSs whose thermal history is rather insensitive to the physics of matter in the stellar cores but is mainly regulated by the magnetic field strength and the amount of accreted material in the heat-blanketing envelopes, as well as by the singlet-state pairing of neutrons in the inner stellar crusts. We show that these cooling regulators are important for explaining the observations of thermal radiation from the isolated NSs hottest for their ages, RX J0822–43 and PSR B1055–52. Our analysis indicates that all realistic microscopic models of the singlet-state neutron pairing are currently consistent with the observations of PSR B1055–52. Adopting these models and tuning the strength of the magnetic field and/or the mass of accreted material, we can also explain the observations of RX J0822–43. We expect that such an interpretation will be refined after new, high-quality observations of RX J0822–43 and PSR B1055–52 appear or new very slowly cooling NSs are discovered. In particular, this will allow one to discriminate between the models of crustal superfluidity and determine the depth of superfluidity disappearance in high-density matter. It will also be possible to constrain the surface magnetic fields and masses of accreted envelopes of these objects. Our results will also be useful for constructing advanced models of cooling NSs, taking into account the evolution of strong surface magnetic fields and the mass of light-element envelopes (e.g., under the action of diffusive nuclear burning).

We believe that the T_b - T_s relation obtained in this paper is reliable at $B \lesssim 10^{14}$ G. The results presented for higher fields are rather indicative, because the dense-plasma effects on the heat conduction by photons near the bottom of the NS photosphere at the superstrong fields have not yet been explored in detail.

We thank Forrest Rogers and Carlos Iglesias for providing the monochromatic opacities and EOS for iron at $B = 0$. We also thank the referee for useful comments. D. G. Y. is indebted to Victor Khodel for the idea to use the models of neutron superfluidity presented in Figure 11 and to George Pavlov for providing the data on PSR B1055–52. The work of A. Y. P. and D. G. Y. was supported in part by RFBR grants 02-02-17668 and 03-07-90200.

APPENDIX

FITTING FORMULAS FOR THE T_b - T_s RELATION

Let $T_{b9} = T_b/10^9$ K, $T_{s6} = T_s/10^6$ K, and $\eta = g_{14}^2 \Delta M/M$, where $g_{14} = g/10^{14}$ cm s $^{-2}$ and ΔM is the mass of accreted light elements from H to O. We assume that $\eta < 10^{-6}$; at larger η the light elements would undergo efficient pycnonuclear burning. The envelope is fully accreted if $\eta = 10^{-6}$ and nonaccreted if $\eta = 0$. Let T_{a6} and T_{Fe6} denote T_{s6} for the fully accreted and nonaccreted envelopes, respectively.

First, consider the case of $B = 0$. In this case, the fit given by equations (A6) and (A7) of Paper I for the nonaccreted envelope remains valid:

$$T_{Fe6}^4 = g_{14} [(7\zeta)^{2.25} + (0.33\zeta)^{1.25}], \quad \zeta = T_{b9} - 10^{-3} g_{14}^{1/4} \sqrt{7T_{b9}}. \quad (\text{A1})$$

TABLE 2
PARAMETERS OF EQUATIONS (A5) AND (A6)

VALUE OF i	IRON ENVELOPE		ACCRETED ENVELOPE	
	a_i	b_i	a_i	b_i
1.....	1.76E-4	159	4.50E-3	172
2.....	0.038	270	0.055	155
3.....	1.5	172	2.0	383
4.....	0.0132	110	0.0595	94
5.....	0.620	0.363	0.328	0.383
6.....	0.318	0.181	0.237	0.367
7.....	2.3E-9	0.50	6.8E-7	2.28
8.....	3	0.619	2	1.690
9.....	0.160	...	0.113	...
10.....	21	...	163	...
11.....	4.7E+5	...	3.4E+5	...

For the fully accreted envelope, we have

$$T_{a6}^4 = (g_{14}(18.1T_{b9})^{2.42}\{0.447 + 0.075(\log_{10} T_b)/[1 + (6.2T_{b9})^4]\} + 3.2T_{b9}^{1.67}T_{Fe6}^4)/(1 + 3.2T_{b9}^{1.67}). \quad (A2)$$

This fit differs from the equations in Appendix C of Paper I by the correction factor in curly brackets. The difference is most appreciable at $T_b > 10^8$ K, as explained in § 3.1 (see Fig. 6).

Next, consider the fully accreted and nonaccreted magnetized envelopes. In both cases, we can write

$$T_{Fe6,a6}(B) = T_{Fe6,a6}(0)\mathcal{X}, \quad (A3)$$

where the magnetic correction factor \mathcal{X} depends on B , T_b , and θ . It can be fitted by

$$\mathcal{X} = (\mathcal{X}_{\parallel}^{\alpha} \cos^2 \theta + \mathcal{X}_{\perp}^{\alpha} \sin^2 \theta)^{1/\alpha}, \quad \alpha = \begin{cases} 4 + \sqrt{\mathcal{X}_{\perp}/\mathcal{X}_{\parallel}} & \text{for } T_{Fe6}, \\ (2 + \mathcal{X}_{\perp}/\mathcal{X}_{\parallel})^2 & \text{for } T_{a6}, \end{cases} \quad (A4)$$

$$\mathcal{X}_{\parallel} = \left[1 + \frac{a_1 + a_2 T_{b9}^{a_3}}{T_{b9}^2 + a_4 T_{b9}^{a_5}} \frac{B_{12}^{a_6}}{(1 + a_7 B_{12}/T_{b9}^{a_8})^{a_9}} \right] \left[1 + \frac{1}{3.7 + (a_{10} + a_{11} B_{12}^{-3/2}) T_{b9}^2} \right]^{-1}, \quad (A5)$$

$$\mathcal{X}_{\perp} = \frac{[1 + b_1 B_{12}/(1 + b_2 T_{b9}^{b_7})]^{1/2}}{[1 + b_3 B_{12}/(1 + b_4 T_{b9}^{b_8})]^{\beta}}, \quad \beta = (1 + b_5 T_{b9}^{b_6})^{-1}, \quad (A6)$$

with the parameters a_i and b_i given in Table 2.

Finally, the surface temperature of a partly accreted envelope is approximately reproduced by the interpolation

$$T_s = [\gamma T_{a6}^4 + (1 - \gamma) T_{Fe6}^4]^{1/4}, \quad (A7a)$$

$$\gamma = [1 + 3.8(0.1\xi)^9]^{-1} [1 + 0.171\xi^{7/2} T_{b9}]^{-1}, \quad \xi = -\log_{10}(10^6 \eta). \quad (A7b)$$

These fitting formulas have been checked against calculations for input parameters restricted by the conditions $6.5 < \log_{10} T_b/\text{K} < 9.5$, $\log_{10} T_s/\text{K} > 5.3$, and $10 < \log_{10} B/\text{G} < 16$. The numerical values of T_s are reproduced with rms residuals of 3%–5% (<2% for fully accreted envelopes at $\theta = 0$) and maximum deviations within $\approx 20\%$ (within 13% for $\theta = 0$, within 12% for fully accreted or nonaccreted envelopes at any θ , and within 5.2% for fully accreted envelopes at $\theta = 0$).

We emphasize that our numerical results, and hence the fitting formulas given here, are uncertain for superstrong fields ($B > 10^{14}$ G) because of the dense-plasma effects discussed in § 3.3 (see the right-hand panel of Fig. 4). A thorough study of the radiative heat conduction at $\omega < \omega_{\text{pl}}$ is needed to obtain a reliable T_b - T_s relation at such field strengths.

REFERENCES

- Ainsworth, T. L., Wambach, J., & Pines, D. 1989, *Phys. Lett. B*, 222, 173
Arendt, R. G., Dwek, E., & Petre, R. 1991, *ApJ*, 368, 474
Baiko, D. A., Kaminker, A. D., Potekhin, A. Y., & Yakovlev, D. G. 1998, *Phys. Rev. Lett.*, 81, 5556
Bejger, M., Yakovlev, D. G., & Gnedin, O. Y. 2003, *Acta Phys. Polonica B*, 34, 221
Brown, E. F., Bildsten, L., & Chang, P. 2002, *ApJ*, 574, 920
Chabrier, G., Potekhin, A. Y., & Yakovlev, D. G. 1997, *ApJ*, 477, L99
Chang, P., & Bildsten, L. 2003, *ApJ*, 585, 464
Chen, J. M. C., Clark, J. W., Davé, R. D., & Khodel, V. V. 1993, *Nucl. Phys. A*, 555, 59
Chen, J. M. C., Clark, J. W., Krotscheck, E., & Smith, R. A. 1986, *Nucl. Phys. A*, 451, 509
Cohen, R., Lodenquai, J., & Ruderman, M. 1970, *Phys. Rev. Lett.*, 25, 467
Ginzburg, V. L. 1970, *The Propagation of Electromagnetic Waves in Plasmas* (2d ed.; London: Pergamon)
Ginzburg, V. L., & Ozernoy, L. M. 1964, *Zh. Eksp. Teor. Fiz.*, 47, 1030 (English transl., *Sov. Phys.-JETP*, 20, No. 3)
Gnedin, O. Y., Yakovlev, D. G., & Potekhin, A. Y. 2001, *MNRAS*, 324, 725
Greenstein, G., & Hartke, G. J. 1983, *ApJ*, 271, 283
Gudmundsson, E. H., Pethick, C. J., & Epstein, R. I. 1983, *ApJ*, 272, 286
Hernquist, L. 1985, *MNRAS*, 213, 313
Heyl, J. S., & Hernquist, L. 1997a, *ApJ*, 489, L67
———. 1997b, *ApJ*, 491, L95
———. 1998, *MNRAS*, 300, 599

- Heyl, J. S., & Hernquist, L. 2001, *MNRAS*, 324, 292
- Iglesias, C. A., & Rogers, F. J. 1996, *ApJ*, 464, 943
- Kaminker, A. D., Haensel, P., & Yakovlev, D. G. 2001, *A&A*, 373, L17
- Kaminker, A. D., Yakovlev, D. G., & Gnedin, O. Y. 2002, *A&A*, 383, 1076
- Kourganoff, V. 1948, *Astrophysica Norvegica*, 5, 1
- Lai, D., & Salpeter, E. E. 1997, *ApJ*, 491, 270
- Lombardo, U., & Schulze, H.-J. 2001, in *Physics of Neutron Star Interiors*, ed. D. Blaschke, N. Glendenning, & A. Sedrakian (LNP 578; Berlin: Springer), 30
- Mineo, T., Massaro, E., Cusumano, G., & Becker, W. 2002, *A&A*, 392, 181
- Nomoto, K., & Tsuruta, S. 1987, *ApJ*, 312, 711
- Page, D. 1995, *ApJ*, 442, 273
- . 1997, *ApJ*, 479, L43
- . 1998, in *The Many Faces of Neutron Stars*, ed. R. Buccheri, J. van Paradijs, & M. A. Alpar (Dordrecht: Kluwer), 539
- Page, D., & Applegate, J. H. 1992, *ApJ*, 394, L17
- Pavlov, G. G., Shibano, Yu. A., Zavlin, V. E., & Meyer, R. D. 1995, in *The Lives of the Neutron Stars*, ed. M. A. Alpar, Ü. Kiziloğlu, & J. van Paradijs (NATO ASI Ser. C, 450; Dordrecht: Kluwer), 71
- Pavlov, G. G., Zavlin, V. E., & Sanwal, D. 2002, in *270th WE-Heraeus Seminar on Neutron Stars, Pulsars, and Supernova Remnants*, ed. W. Becker, H. Lesch, & J. Trümper (MPE Rep. 278; Garching: MPE), 273
- Pethick, C. J. 1992, *Rev. Mod. Phys.*, 64, 1133
- Potekhin, A. Y. 1999, *A&A*, 351, 787
- Potekhin, A. Y., Baiko, D. A., Haensel, P., & Yakovlev, D. G. 1999a, *A&A*, 346, 345
- Potekhin, A. Y., & Chabrier, G. 2000, *Phys. Rev. E*, 62, 8554
- . 2003, *ApJ*, 585, 955
- Potekhin, A. Y., Chabrier, G., & Shibano, Yu. A. 1999b, *Phys. Rev. E*, 60, 2193 (erratum 63, 019901 [2001])
- Potekhin, A. Y., Chabrier, G., & Yakovlev, D. G. 1997, *A&A*, 323, 415 (Paper I)
- Potekhin, A. Y., & Yakovlev, D. G. 2001, *A&A*, 374, 213 (Paper II)
- Prakash, M., Ainsworth, T. L., & Lattimer, J. M. 1988, *Phys. Rev. Lett.*, 61, 2518
- Rajagopal, M., Romani, R. W., & Miller, M. C. 1997, *ApJ*, 479, 347
- Rogers, F. J., Swenson, F. J., & Iglesias, C. A. 1996, *ApJ*, 456, 902
- Sahriling, M., & Chabrier, G. 1998, *ApJ*, 493, 879
- Schaaf, M. E. 1990a, *A&A*, 227, 61
- . 1990b, *A&A*, 235, 499
- Schatz, H., et al. 2001, *Phys. Rev. Lett.*, 86, 3471
- Schulze, H.-J., Cugnon, J., Lejeune, A., Baldo, M., & Lombardo, U. 1996, *Phys. Lett. B*, 375, 1
- Shibano, Yu. A., & Yakovlev, D. G. 1996, *A&A*, 309, 171
- Silant'ev, N. A., & Yakovlev, D. G. 1980, *Ap&SS*, 71, 45
- Thorne, K. S. 1977, *ApJ*, 212, 825
- Thorolfsson, A., Rögnvaldsson, Ö. E., Yngvason, J., & Gudmundsson, E. H. 1998, *ApJ*, 502, 847
- Tsuruta, S., Canuto, V., Lodenquai, J., & Ruderman, M. 1972, *ApJ*, 176, 739
- Ushomirsky, G., & Rutledge, R. E. 2001, *MNRAS*, 325, 1157
- Van Riper, K. A. 1988, *ApJ*, 329, 339
- . 1991, *ApJS*, 75, 449
- Ventura, J., & Potekhin, A. Y. 2001, in *The Neutron Star-Black Hole Connection*, ed. C. Kouveliotou, J. Ventura, & E. P. J. van den Heuvel (NATO ASI Ser. C, 567; Dordrecht: Kluwer), 393
- Walter, F. M., & Lattimer, J. M. 2002, *ApJ*, 576, L145
- Wambach, J., Ainsworth, T. L., & Pines, D. 1993, *Nucl. Phys. A*, 555, 128
- Winkler, P. F., Tuttle, J. H., Kirshner, R. P., & Irwin, M. J. 1988, in *IAU Colloq. 101, Supernova Remnants and the Interstellar Medium*, ed. R. S. Roger & T. L. Landecker (Cambridge: Cambridge Univ. Press), 65
- Yakovlev, D. G., Gnedin, O. Y., Kaminker, A. D., & Potekhin, A. Y. 2002a, in *270th WE-Heraeus Seminar on Neutron Stars, Pulsars, and Supernova Remnants*, ed. W. Becker, H. Lesch, & J. Trümper (MPE Rep. 278; Garching: MPE), 287
- Yakovlev, D. G., & Kaminker, A. D. 1994, in *IAU Colloq. 147, The Equation of State in Astrophysics*, ed. G. Chabrier & E. Schatzman (Cambridge: Cambridge Univ. Press), 214
- Yakovlev, D. G., Kaminker, A. D., & Gnedin, O. Y. 2001, *A&A*, 379, L5
- Yakovlev, D. G., Kaminker, A. D., Haensel, P., & Gnedin, O. Y. 2002b, *A&A*, 389, L24
- Yakovlev, D. G., Levenfish, K. P., & Shibano, Yu. A. 1999, *Phys.-Uspekhi*, 42, 737
- Yakovlev, D. G., & Urpin, V. A. 1980, *Soviet Astron.*, 24, 303
- Zavlin, V. E., Trümper, J., & Pavlov, G. G. 1999, *ApJ*, 525, 959